The Spherical Harmonics Expansion Method for Assessing Hot Carrier Degradation

Markus Bina and Karl Rupp

Abstract An overview of recent developments for solving the Boltzmann transport equation for semiconductors in a deterministic manner using spherical harmonics expansions is given. The method is an attractive alternative to the Monte Carlo method, since it does not suffer from inherent stochastic limitations such as the difficulty of resolving small currents, excessive execution times, or the inability to deal with rare events such as tunneling or low-frequency noise. In particular, the method allows for a resolution of the high-energy tail of the distribution function free from stochastic noise, which makes it very attractive for hot carrier degradation. We review recent improvements to the method and compare results obtained for a 250 nm and a 25 nm MOSFET, demonstrating the importance of electron-electron scattering in scaled-down devices.

1 Introduction

Previous chapters in this book, most notably Chaps. 5 and 8 [1,2], already discussed in detail how high electric fields, as they are common in the pinch-off region of a MOSFET, lead to an acceleration of a substantial number of carriers to high kinetic energies. In particular, a few carriers may even reach energies up to several electron Volts, which is sufficient for breaking atomic bonds or for surpassing the energy barrier of the gate oxide. Damage caused to the crystal lattice by such highly energetic carriers can be irreversible, hence these so-called *hot carriers* are of utmost interest for the study of device degradation phenomena. Assuming that a stationary distribution of carriers $f(\boldsymbol{x}, \varepsilon, t)$ with respect to the spatial location $\boldsymbol{x}$ as well as energy ε and time t is known, the study of hot carrier degradation (HCD) is primarily interested in the so-called high-energy tail of the carrier energy distribution [3], i.e. the distribution of carriers at high kinetic energies. Modeling the

M. Bina • K. Rupp (✉)
Institute for Microelectronics, TU Wien, Gußhausstraße 27–29, 1040 Wien, Austria
e-mail: bina@iue.tuwien.ac.at; rupp@iue.tuwien.ac.at

T. Grasser (ed.), *Hot Carrier Degradation in Semiconductor Devices*,
DOI 10.1007/978-3-319-08994-2_6

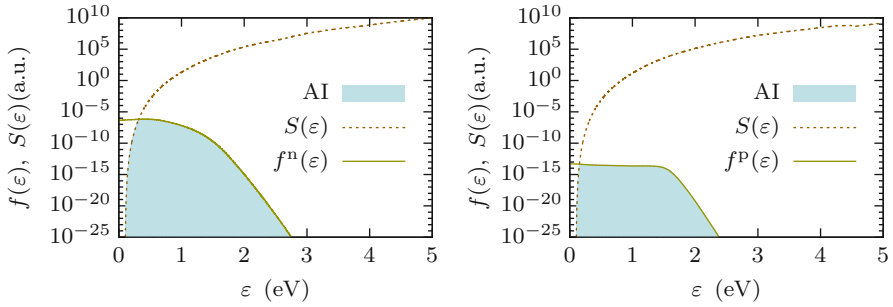

Fig. 1 Exemplary distribution functions and acceleration integrals (*shaded area*) for electrons (*left*) and holes (*right*) in the middle of an artificial short channel (25 nm) n-channel MOSFET. The importance of the high-energy tail due to the rapid increase in the collision cross section $S(\varepsilon)$ for the calculation of the acceleration integral is readily visible

eventual damage caused by a carrier at energy ε through a so-called capture cross section $S(\varepsilon)$, the total rate $G(\boldsymbol{x}, t)$ is obtained from the acceleration integral (AI)

$$G(\boldsymbol{x}, t) \sim \int_0^\infty f(\boldsymbol{x}, \varepsilon, t) S(\varepsilon)\, \mathrm{d}\varepsilon.$$

Typically, the capture cross section is assumed to vanish below a certain threshold energy $\varepsilon^{\mathrm{th}}$:

$$G(\boldsymbol{x}, t) \sim \int_{\varepsilon^{\mathrm{th}}}^\infty f(\boldsymbol{x}, \varepsilon, t) S(\varepsilon)\, \mathrm{d}\varepsilon, \tag{1}$$

Although secondary carrier generation requires a kinetic energy of the primary particle above the band gap energy, $\varepsilon^{\mathrm{th}}$ generally takes values below the band gap energy to include effects other than secondary carrier generation. Above $\varepsilon^{\mathrm{th}}$, the capture cross section $S(\varepsilon)$ grows quickly [4]. Thus, the distribution function needs to be computed accurately at higher energies, which mandates the consideration of appropriate scattering mechanisms [3, 5] including carrier-carrier scattering and impact ionization [5, 6] (cf. Fig. 1). The remainder of this chapter will thus focus on the accurate computation of the carrier distribution function, whereas more elaborate studies of HCD based on the availability of the high-energy tail of the distribution function can be found especially in Chaps. 5, 7, 10, and 13 [1, 2, 7, 8].

The governing equation for the aforementioned carrier distribution function, the Boltzmann Transport Equation (BTE), is discussed in Sect. 2. A deterministic solution method by means of spherical harmonics expansions is then presented in Sect. 3. The various physical input quantities such as the band structure and the scattering mechanisms are discussed in detail in Sect. 4. Then, Sect. 5 presents HCD simulation results for an n-channel MOSFET. A discussion of not only technical aspects in making the SHE method more accessible to the HCD community is given in Sect. 6. Finally, this chapter closes with a conclusion in Sect. 7.

2 The Boltzmann Transport Equation

The BTE describes the carrier transport subject to the collision-less, free flight in response to an external force, as well as scattering with other carriers or the crystal lattice. The free flight of charge carriers in the lattice is described by the equations of motion (Newton's law)

$$\hbar \partial_t \boldsymbol{k}' = \boldsymbol{F} \quad \text{and} \quad \partial_t \boldsymbol{x} = \boldsymbol{v}, \tag{2}$$

where the relation $\boldsymbol{p} = \hbar \boldsymbol{k}'$ coupling the momentum $\boldsymbol{p}$ with the wave vector $\boldsymbol{k}'$ is employed. The collisions between carriers and the lattice is described by quantum mechanical perturbation theory (Fermi's Golden Rule). It has to be noted that in the classical framework of the BTE, where Heisenberg's uncertainty principle is neglected, both position and momentum of each carrier can be tracked precisely. However, tracking each particle individually in a classical approach is computationally infeasible, therefore the spatial and temporal evolution of particles is condensed into an ensemble distribution function $f(\boldsymbol{x}, \boldsymbol{k}', t)$, which is defined such that

$$\mathrm{d}N = \frac{2}{(2\pi)^3} f \, \mathrm{d}^3x \, \mathrm{d}^3k' \tag{3}$$

is the number of carriers in the infinitesimal small volume $\mathrm{d}^3x \, \mathrm{d}^3k'$ in the six-dimensional phase-space at time t. Without going into the details of the derivation, the so-defined distribution function obeys the BTE

$$\frac{\partial f}{\partial t} + \boldsymbol{v} \cdot \nabla_{\boldsymbol{x}} f + \frac{1}{\hbar} \boldsymbol{F} \cdot \nabla_{\boldsymbol{k}'} f = \mathcal{Q}\{f\} + \Gamma, \tag{4}$$

where $\boldsymbol{v}$ denotes the group velocity,

$$\boldsymbol{F} = -\nabla_{\boldsymbol{x}} (\mathrm{q}\psi + \varepsilon_\mathrm{b}) \tag{5}$$

is the force due to the electrostatic potential ψ, the particle charge q (negative for electrons, positive for holes), and the band edge minimum ε_b. $\mathcal{Q}\{f\}$ refers to the scattering operator and Γ models the generation and recombination of carriers. Magnetic fields can also be included in a straight-forward manner [9], yet will not be considered further in this work. In principle, a BTE needs to be solved for each valley and each carrier type (electrons and holes), where interactions occur through inter-valley scattering and generation-recombination processes. For the sake of simplicity and better readability, the subsequent discussion assumes a single valley for a single carrier type unless noted otherwise and arguments are suppressed whenever appropriate. Since the electrostatic potential ψ is needed in order to compute the force exerted on each charge carrier, one needs to solve Poisson's

equation and the BTE for electrons and holes self-consistently. The full system of equations thus reads

$$\begin{aligned} \nabla \cdot (\varepsilon(\boldsymbol{x})\nabla\psi) &= |\mathrm{q}|(n - p + C), \\ \partial_t f^{\mathrm{n}} + \underbrace{\boldsymbol{v}^{\mathrm{n}} \cdot \nabla_{\boldsymbol{x}} f^{\mathrm{n}} + \hbar^{-1} \boldsymbol{F} \cdot \nabla_{\boldsymbol{k}} f^{\mathrm{n}}}_{=\mathcal{L}^{\mathrm{n}}\{f^{\mathrm{n}}\}} &= \mathcal{Q}^{\mathrm{n}}\{f^{\mathrm{n}}\} - \Gamma^{\mathrm{n}}\{f^{\mathrm{n}}, f^{\mathrm{p}}\}, \\ \partial_t f^{\mathrm{p}} + \underbrace{\boldsymbol{v}^{\mathrm{p}} \cdot \nabla_{\boldsymbol{x}} f^{\mathrm{p}} - \hbar^{-1} \boldsymbol{F} \cdot \nabla_{\boldsymbol{k}} f^{\mathrm{p}}}_{=\mathcal{L}^{\mathrm{p}}\{f^{\mathrm{p}}\}} &= \mathcal{Q}^{\mathrm{p}}\{f^{\mathrm{p}}\} - \Gamma^{\mathrm{p}}\{f^{\mathrm{n}}, f^{\mathrm{p}}\}, \end{aligned} \tag{6}$$

where f^{n} and f^{p} denote the electron and hole distribution functions, n and p are the electron and hole concentrations, respectively, and C accounts for fixed charges such as the doping. $\mathcal{L}^{\mathrm{n}}$ and $\mathcal{L}^{\mathrm{p}}$ are the so-called free streaming operators for electrons and holes, describing the free flight of carriers.

Without further approximations, each BTE has to be solved in three spatial and three phase space dimensions as well as time. As a consequence, a direct discretization of the full system in such a high-dimensional space results in prohibitive memory requirements and execution times for most applications. Thus, further approximations or alternative discretization schemes have to be employed.

The numerical solution of (6) is traditionally approached by using the Monte Carlo method [10], which is computationally- and time-intensive, particularly when the high-energy tails of the distribution function have to be resolved in detail [11]. As a consequence, first results obtained using the Monte Carlo method for a long-channel MOSFET were reported only recently [4]. Therefore, simplified models not relying on solution of the BTE have been developed in the meanwhile [12, 13], some of which are discussed in Chaps. 5, 6, 11, and 13 in this book [1, 7, 8, 14]. Moreover, the inherent stochastic noise in the high-energy tail of the distribution function computed by the Monte Carlo method may introduce significant errors to the computed rates.

3 Spherical Harmonics Expansion

Macroscopic models obtained from moments of the distribution function are only poorly suited for research on HCD, because the distribution function is no longer accessible directly and has to be recovered through assumptions and approximations. On the other hand, for the reasons discussed in the previous section the Monte Carlo method suffers from limitations inherent to its stochastic nature when applied to the study of HCD. Here we consider the spherical harmonics expansion (SHE) method, which is a deterministic spectral method for solving the BTE and consequently free of stochastic noise. A resolution of the distribution function over a virtually arbitrary scale is possible, rendering the method very attractive for HCD.

In the SHE method, the distribution function is expanded into spherical harmonics $Y^{l,m}$, where the series is truncated at a maximum expansion order $l_{\max}$ [15, 16]. This is motivated by the fact that the distribution of carriers in equilibrium is spherically symmetric and can thus, unlike moment-based methods, be represented exactly by a zeroth-order expansion. Moreover, dispersion relations of semiconductors, particularly silicon, are in good approximation spherical after a suitable scaling of the principal axes of the phase space. More precisely, the elliptical valleys in silicon are mapped onto spherical ones using the Herring-Vogt transform [17] (for each valley)

$$\hat{T} = \begin{pmatrix} T_x & 0 & 0 \\ 0 & T_y & 0 \\ 0 & 0 & T_z \end{pmatrix}$$

from the original $\boldsymbol{k}'$ space to the transformed space via $\boldsymbol{k} = \hat{T}\boldsymbol{k}'$. Consequently, the partial derivatives in the BTE (4) need to take this transformation into account, resulting in

$$\frac{\partial f}{\partial t} + \hat{T}\boldsymbol{v} \cdot \nabla_{\boldsymbol{x}} f + \frac{1}{\hbar}\hat{T}\boldsymbol{F} \cdot \nabla_{\boldsymbol{k}} f = Q\{f\} \tag{7}$$

for the Herring-Vogt-transformed case.

A SHE can in principle be carried out for either constant modulus $k = \|\boldsymbol{k}\|$ of the transformed wave vector, or for constant kinetic energy ε. An expansion with respect to energy has several advantages: For example, the distribution function is isotropic on equienergy surfaces in equilibrium and many scattering rates are a function of energy [18]. Thus, the spherical coordinates (k, θ, φ) in $\boldsymbol{k}$-space are mapped onto spherical coordinates $(\varepsilon, \theta, \varphi)$ in energy space, where we keep the angles unchanged and require the mapping to be unique in both directions [19]. Such a one-to-one mapping is naturally fulfilled for parabolic and nonparabolic models, but not for a full-band model. However, we will see in Sect. 4.1 that the requirement of a one-to-one mapping can be relaxed substantially, allowing for the consideration of a broad range of full-band effects.

An arbitrary function u can be expanded in energy space with spherical coordinates $(\varepsilon, \theta, \varphi)$ as

$$u(\boldsymbol{x}, \boldsymbol{k}(\varepsilon, \theta, \varphi), t) = \sum_{l=0}^{\infty} \sum_{m=-l}^{l} u_{l,m}(\boldsymbol{x}, \varepsilon, t) Y^{l,m}, \tag{8}$$

where $Y^{l,m}$ are the orthonormal, real-valued spherical harmonics on the unit sphere. Conversely, for any given function u on the unit sphere, the expansion coefficient $u_{l,m}$ is obtained from a projection onto the respective spherical harmonic:

$$u_{l,m} = \int_{\partial\Omega} u Y^{l,m} \, \mathrm{d}\Omega \tag{9}$$

Here, Ω denotes the unit sphere and $\mathrm{d}\Omega = \sin\theta \, \mathrm{d}\theta \, \mathrm{d}\varphi$. The description of the BTE in $\boldsymbol{k}$-space requires a projection of a function u to be applied over the whole Brillouin zone $\mathcal{B}$ for a given energy ε as

$$\frac{1}{(2\pi)^3} \int_{\mathcal{B}} \delta(\varepsilon - \varepsilon(\boldsymbol{k})) Y^{l,m} u \, \mathrm{d}\boldsymbol{k}, \tag{10}$$

resulting after a change to spherical variables in

$$\int_{\partial\Omega} Y^{l,m} u Z(\varepsilon, \theta, \varphi) \, \mathrm{d}\Omega, \tag{11}$$

where the generalized density of states Z is obtained from the Jacobian of the coordinate transformation as

$$Z(\varepsilon, \theta, \varphi) = \frac{k^2}{(2\pi)^3} \frac{\partial k}{\partial \varepsilon}. \tag{12}$$

This generalized density of states differs from the conventional density of states by a factor of 4π, which is obtained in the spherically symmetric case by an integration over the angles θ and φ. The important detail in (11) is the generalized density of states entering the integrand in the course of the projection. If it is taken to be spherically symmetric, i.e. $Z(\varepsilon, \theta, \varphi) = Z(\varepsilon)$, then (9) and (11) differ only by a constant factor for a fixed kinetic energy ε. On the other hand, a full angular dependence of Z will lead to unrelated expansion coefficients obtained from (9) and (11) in general.

Since the distribution function f is a-priori unknown and only known to fulfill the BTE, a system of equations for the expansion coefficients needs to be derived from the BTE. This system is obtained by projecting (7) onto the spherical harmonics $Y^{l,m}$. For details of the derivation we refer to the literature [18] and directly state the resulting set of equations:

$$\frac{\partial g_{l,m}}{\partial t} + \frac{\partial (\boldsymbol{F} \cdot \hat{\boldsymbol{j}}_{l,m})}{\partial \varepsilon} + \nabla_{\boldsymbol{x}} \cdot \hat{\boldsymbol{j}}_{l,m} - \hat{T} \boldsymbol{F} \cdot \boldsymbol{\Gamma}_{l,m} = Q_{l,m}\{g\}, \tag{13}$$

where we set $g := fZ$ motivated by (11), $\hat{\boldsymbol{j}}$ is the generalized current density given by

$$\hat{\boldsymbol{j}}_{l,m} = \int_{\partial\Omega} \hat{T} \boldsymbol{v} g Y^{l,m} \, \mathrm{d}\Omega, \tag{14}$$

and

$$\boldsymbol{\Gamma}_{l,m} = \int_{\partial\Omega} \frac{g}{\hbar k} \left(\frac{\partial Y^{l,m}}{\partial \theta} \boldsymbol{e}_\theta + \frac{1}{\sin\theta} \frac{\partial Y^{l,m}}{\partial \varphi} \boldsymbol{e}_\varphi \right) \mathrm{d}\Omega \tag{15}$$

with unit vectors $\boldsymbol{e}_\theta$ and $\boldsymbol{e}_\varphi$ in the spherical coordinate system for the θ and φ directions, respectively. The projected scattering operator $Q_{l,m}\{g\}$ will be discussed below. To better expose the structure of the equations, we combine $\nabla_{\boldsymbol{x}}$ and $\partial/\partial\varepsilon$ to yield a divergence in $(\boldsymbol{x}, \varepsilon)$-space:

$$\frac{\partial g_{l,m}}{\partial t} + \nabla_{\boldsymbol{x},\varepsilon} \cdot \tilde{\boldsymbol{j}}_{l,m} - \hat{T}\boldsymbol{F} \cdot \boldsymbol{\Gamma}_{l,m} = Q_{l,m}, \tag{16}$$

with

$$\tilde{\boldsymbol{j}}_{l,m} = \begin{pmatrix} \hat{\boldsymbol{j}}_{l,m} \\ \boldsymbol{F} \cdot \hat{\boldsymbol{j}}_{l,m} \end{pmatrix}. \tag{17}$$

Similar to numerical solution techniques based on Fourier series, we substitute a SHE truncated at finite expansion order $l'_{\max}$ for g as

$$g \approx \sum_{l'=0}^{l'_{\max}} \sum_{m'=-l'}^{l'} g_{l',m'} Y^{l',m'}. \tag{18}$$

As indicated in Fig. 2, values between one and five are common choices for $l'_{\max}$ for practical purposes. For a more compact notation we employ Einstein's summation convention for repeated upper and lower indices to write

$$\hat{\boldsymbol{j}}_{l,m} = \hat{\boldsymbol{v}}_{l,m}^{l',m'} g_{l',m'}, \tag{19}$$

$$\boldsymbol{\Gamma}_{l,m} = \boldsymbol{\Gamma}_{l,m}^{l',m'} g_{l',m'}, \tag{20}$$

with

$$\hat{\boldsymbol{v}}_{l,m}^{l',m'} = \int_{\partial\Omega} \hat{T}\boldsymbol{v} Y^{l',m'} Y^{l,m} \,\mathrm{d}\Omega, \tag{21}$$

$$\boldsymbol{\Gamma}_{l,m}^{l',m'} = \int_{\partial\Omega} \frac{Y^{l',m'}}{\hbar k} \left(\frac{\partial Y^{l,m}}{\partial\theta} \boldsymbol{e}_\theta + \frac{1}{\sin\theta} \frac{\partial Y^{l,m}}{\partial\varphi} \boldsymbol{e}_\varphi \right) \mathrm{d}\Omega. \tag{22}$$

After splitting the scattering operator into in-scattering and out-scattering contributions via $\mathcal{Q}\{g\} = \sum_\eta Q_\eta\{g\}^{\text{in}} - Q_\eta\{g\}^{\text{out}}$ for each scattering process identified by η, a projection and insertion of (18) results in

$$\begin{aligned} &\frac{\partial g_{l,m}}{\partial t} + \nabla_{\boldsymbol{x},\varepsilon} \cdot \tilde{\boldsymbol{j}}_{l,m}^{l',m'} g_{l',m'} - \boldsymbol{F} \cdot \boldsymbol{\Gamma}_{l,m}^{l',m'} g_{l',m'} \\ &\quad = \sum_\eta \left[Q_{\eta;l,m}^{\text{in};l',m'} g_{l',m'}(\boldsymbol{x}, \varepsilon \mp \hbar\omega_\eta, t) - Q_{\eta;l,m}^{\text{out};l',m'} g_{l',m'} \right], \end{aligned} \tag{23}$$

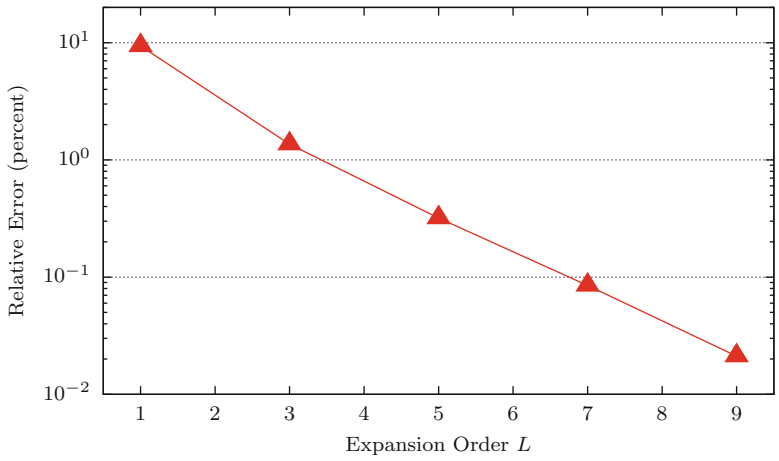

Fig. 2 Comparison of the relative error in the collector current of a silicon-germanium heterojunction bipolar transistor for different SHE orders [20]. First-order expansions show an error of 10 % compared to an eleventh-order expansion, which may be unacceptable for scaled-down devices

where the (possibly vanishing) inelastic energy transfer involved in the scattering process identified by η is $\hbar\omega_\eta$. Equation (23) defines a system of $(l_{\max}+1)^2$ coupled first-order partial differential equations with shifted arguments $\varepsilon \mp \hbar\omega_\eta$ for the in-scattering term to be solved in order to determine the unknown expansion coefficients $g_{l,m}$. The system is posed in the five-dimensional $(\boldsymbol{x}, \varepsilon, t)$-space rather than the seven-dimensional $(\boldsymbol{x}, \boldsymbol{k}, t)$-space of the BTE, hence reducing the computational burden substantially. Moreover, for stationary simulations the solution space reduces to four dimensions (or three and two dimensions for two- or one-dimensional device simulations, respectively). This reduction of dimensionality of the computational domain makes the SHE method particularly attractive.

3.1 Boundary Conditions

The system of equations (23) needs to be supplemented with suitable boundary conditions in order to fully specify the equation system. At non-contact boundaries, homogeneous Neumann boundary conditions are applied just like for the drift-diffusion system. Similarly, homogeneous Neumann boundary conditions are applied at the energy boundaries $\varepsilon = 0$ and $\varepsilon = \varepsilon_{\max}$, if the considered kinetic energy range for the simulation is limited by some maximum kinetic energy $\varepsilon_{\max}$. Scattering processes with initial or final energy outside the considered energy range, including scatter events to or from the band gap, are suppressed. Early publications

imposed Maxwell–Boltzmann distributions f^{eq} via Dirichlet boundary conditions of the form

$$f_{l,m}(\varepsilon) = \begin{cases} f^{\mathrm{eq}} := M \exp\left(-\frac{\varepsilon}{k_{\mathrm{B}}T}\right), & l = m = 0, \\ 0 & \text{otherwise.} \end{cases} \tag{24}$$

at the contacts, where k_{B} is the Boltzmann constant, T denotes temperature, and M is a suitable normalization factor in order to obtain the correct contact carrier density. While such a thermal equilibrium assumption is reasonable at the inflow contacts, it leads to boundary layers at the outflow-contact at higher bias [21], forcing a heated carrier distribution to thermal equilibrium. This deficiency is addressed by a generation/recombination process with rate

$$\gamma_{l,m} = -\frac{g_{l,m} - Z_{l,m} f^{\mathrm{eq}}_{l,m}}{\tau_0}, \tag{25}$$

where $Z_{l,m}$ is the spherical harmonics expansion coefficient of the generalized density of states, $f^{\mathrm{eq}}_{l,m}$ is the (l,m)-th expansion coefficient of the equilibrium (Maxwell–Boltzmann) distribution as in (24), and τ_0 is the recombination time [18, 21]. Here, τ_0 provides control over the difference between thermal equilibrium and the computed solution. In the limit $\tau_0 \to 0$ the Dirichlet boundary condition (24) is recovered. Practical values for τ_0 are in the femtosecond range.

A parameter-free improvement of (25) was introduced by Hong et al. [9], where a surface generation rate of the form

$$\gamma^{\mathrm{s}}(\boldsymbol{k}') = -\left[f^{\mathrm{eq}} \mathbb{1}_{[0,\infty)}(-\hat{T}\boldsymbol{v}\cdot\boldsymbol{n}) + f\,\mathbb{1}_{[0,\infty)}(\hat{T}\boldsymbol{v}\cdot\boldsymbol{n})\right]\hat{T}\boldsymbol{v}\cdot\boldsymbol{n} \tag{26}$$

with outward pointing unit normal vector $\boldsymbol{n}$ at the contact and the Heaviside step function $\mathbb{1}_{[0,\infty)}$ was proposed. Here, the first term describes carriers in thermal equilibrium entering the device ($\hat{T}\boldsymbol{v}$ to point into the device), while the second term describes the annihilation of heated carriers leaving the device. Such a boundary condition corresponds to a thermal bath contact as used in Monte Carlo simulations [10].

3.2 Stabilization and H-Transform

The partial derivatives with respect to the spatial variable $\boldsymbol{x}$ as well as the kinetic energy ε in (23) describe the motion of carriers in free flight. In the absence of scattering mechanisms, carriers solely gain or lose kinetic energy in reaction to the force term $\boldsymbol{F}$, hence the trajectories of carriers in free flight in $(\boldsymbol{x}, \varepsilon)$-space mirror the potential profile throughout the device. Regular discretizations with respect to the kinetic energy ε are unable to trace these trajectories accurately, hence

numerical instabilities show up if no special measures are applied. Rahmat et al. used a semi-empirical upwind-scheme to stabilize the equations for the simulation of devices in the micrometer regime [22]. Jungemann et al. applied the maximum entropy dissipation scheme (MEDS) [23] and obtained good numerical stability for devices of about 100 nm length. As ballistic transport becomes increasingly dominant for smaller devices, the so-called H-transformation [24] was considered in addition to MEDS in [9] and due to its superior numerical stability used in all subsequent publications. The essence of the H-transformation is to apply a change of coordinates from kinetic energy ε to total energy $H = \varepsilon - \mathrm{q}\psi(\boldsymbol{x})$, through which the derivative with respect to energy in (23) vanishes and one obtains

$$\frac{\partial g_{l,m}}{\partial t} + \nabla_{\boldsymbol{x}} \cdot \hat{\boldsymbol{j}}_{l,m}^{l',m'} g_{l',m'} - \hat{T}\boldsymbol{F} \cdot \boldsymbol{\Gamma}_{l,m}^{l',m'} g_{l',m'} = \sum_{\eta} \left[Q_{\eta;l,m}^{\mathrm{in};l',m'} g_{l',m'}(\boldsymbol{x}, H \mp \hbar\omega_{\eta}, t) - Q_{\eta;l,m}^{\mathrm{out};l',m'} g_{l',m'} \right]. \tag{27}$$

For simplicity the variable names were reused, even though all quantities are now a function of $(\boldsymbol{x}, H, t)$ instead of $(\boldsymbol{x}, \varepsilon, t)$. Carrier trajectories are now given by constant total energy H and are well resolved when using a regular grid with respect to the total energy coordinate, cf. Fig. 3. The price to pay for the high numerical stability is the dependence of the band edge on the potential, hence the simulation regions for the conduction and valence bands need to be recomputed after each change of the potential. MEDS applied to the H-transformed equations results in the multiplication of the equations by a constant, hence can be omitted. On the other hand, a scaling of the equations in accordance to MEDS results in an M-matrix property of the system matrix for a first-order SHE method, which simplifies the solution process and ensures positivity of the solution [9].

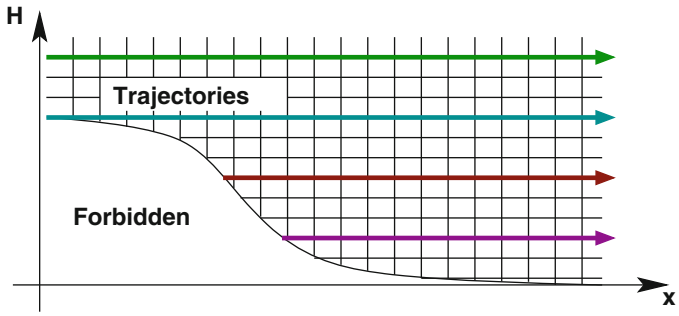

Fig. 3 The H-transformation results in carrier trajectories under free flight to be given by constant total energy H. Scattering mechanisms couple the individual trajectories. The shape of the band edge is determined by the material configuration and the electrostatic potential

4 Physics

During the presentation of the SHE method in Sect. 3 a discussion of additional material-specific properties or physical details has been set aside wherever possible. However, such details are essential for predictive device simulation, yet require a careful analysis to match the underlying material well. In this section we discuss these details in more depth. Because of its high technological relevance, results are primarily given for silicon.

4.1 Band Structure

From the dispersion relation $\varepsilon(\boldsymbol{k})$ one can fully describe the ballistic transport of carriers in a device. More precisely, both the group velocity $\nabla_{\boldsymbol{x}}\varepsilon/\hbar$ and the density of states (12) are directly obtained. During the derivation of the SHE method we have required that the mapping from ε to k is one-to-one, hence the term $1/(\hbar k)$ in (27) can be evaluated directly. For the common analytical band structure models, namely the parabolic band structure

$$\varepsilon^{\text{parabolic}}(\boldsymbol{k}) = \frac{\hbar^2 k^2}{2m^*} \tag{28}$$

with effective mass m^* and the non-parabolic modification [25, 26]

$$\varepsilon'(1 + \alpha\varepsilon') = \frac{\hbar^2 k^2}{2m^*} \tag{29}$$

these one-to-one mappings are obtained directly. Similarly, the dispersion relation can be inverted for each band of the many-band model for silicon [27]. These models typically reproduce the density of states as well as the group velocity fairly well at energies below 1 eV, but fail to provide good approximations at higher energies. Thus, they are generally not suitable to assess hot carrier degradation, where energies above 1 eV are common.

A better approximation of the dispersion relation can in principle be obtained from a SHE of the inverse dispersion relation

$$k(\varepsilon, \theta, \varphi) = \sum_{l=0}^{l^{\text{k}}_{\text{max}}} \sum_{m=-l}^{l} k_{l,m} Y^{l,m} \tag{30}$$

for some maximum expansion order $l^{\text{k}}_{\text{max}}$. Such an approach was pursued by Kosina et al. [19] for the valence band up to an energy of 1.27 eV and later refined by Pham et al. [28]. Subsequently, a fitted band structure based on the SHE of the conduction

band has also been developed [29]. However, a systematic error cannot be avoided because of the requirement of a one-to-one-mapping between the kinetic energy ε and the modulus of the wave vector k.

Vecchi et al. [30] found that the equations for a first-order SHE can be recast such that the term $\mathbf{\Gamma}_{l,m}$ as defined in (15) does not contribute, hence the explicit one-to-one mapping is no longer necessary after the projection. Thus, even though such a one-to-one mapping is formally required for the derivation of the SHE method, one can directly use full-band data for the modulus of the wave-vector and the density of states in the final equations. Jin et al. [31] extended this approach to arbitrary-order expansions by observing that under the assumption of spherically symmetric dispersion relations one can rewrite

$$2\frac{Z}{\hbar k} = \frac{\partial v Z}{\partial \varepsilon} \tag{31}$$

and reuse this to eliminate the explicit dependence on k in (15). With this and the direct use of full-band data for v and Z as depicted in Fig. 4, good agreement with results from full-band Monte Carlo simulations was obtained. As a consequence, the extended Vecchi model is also well-suited for the study of HCD. Hong et al. [16] proposed a further refinement of this approach in order to eliminate or reduce the remaining systematic differences in the band description. The key of the derivation is to postpone the isotropic valley approximation in the approaches by Vecchi et al. and Jin et al. until the last stage of the model derivation. While the first conduction band is treated rigorously for increased accuracy, higher conduction bands are approximated using the isotropic model, leading to a slight overall improvement in accuracy.

4.2 Pauli Principle

The scattering operator for scattering events other than carrier-carrier scattering is often written in a low-density approximation as

$$\mathcal{Q}\{f\} = \frac{1}{(2\pi)^3}\int_{\mathcal{B}} s(\boldsymbol{x},\boldsymbol{k}^*,\boldsymbol{k})\, f(\boldsymbol{x},\boldsymbol{k}^*,t) - s(\boldsymbol{x},\boldsymbol{k},\boldsymbol{k}^*)\, f(\boldsymbol{x},\boldsymbol{k},t)\,\mathrm{d}\boldsymbol{k}^* \tag{32}$$

with scattering rate $s(\boldsymbol{x},\boldsymbol{k}^{\text{initial}},\boldsymbol{k}^{\text{final}})$ for a scattering process from an initial state $\boldsymbol{k}^{\text{initial}}$ to a final state $\boldsymbol{k}^{\text{final}}$. However, most states at low energy may be occupied at high carrier densities, hence the Pauli exclusion principle must not be neglected and the full scattering operator

$$\begin{aligned}\mathcal{Q}\{f\} = \frac{1}{(2\pi)^3}\int_{\mathcal{B}} & s(\boldsymbol{x},\boldsymbol{k}^*,\boldsymbol{k})\, f(\boldsymbol{x},\boldsymbol{k}^*,t)\big(1 - f(\boldsymbol{x},\boldsymbol{k},t)\big) \\ & - s(\boldsymbol{x},\boldsymbol{k},\boldsymbol{k}^*)\, f(\boldsymbol{x},\boldsymbol{k},t)\big(1 - f(\boldsymbol{x},\boldsymbol{k}^*,t)\big)\,\mathrm{d}\boldsymbol{k}^*\end{aligned} \tag{33}$$

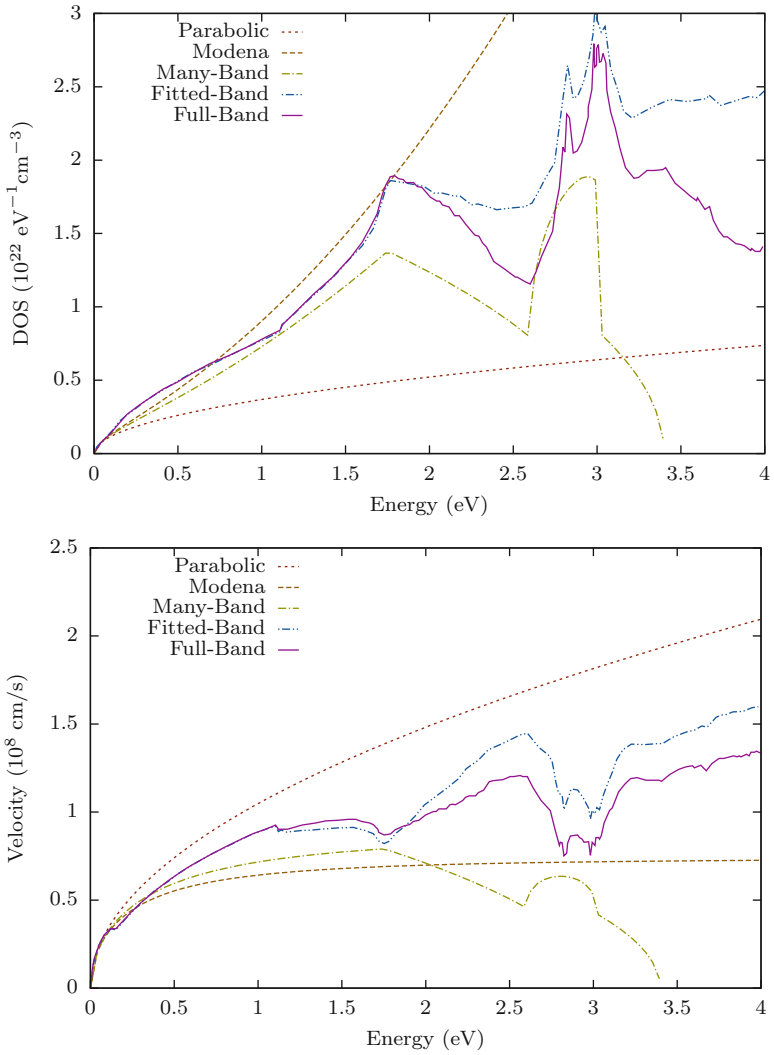

Fig. 4 Comparison of the density of states Z and the group velocity v for different dispersion relations commonly used with the SHE method

needs to be considered, cf. Fig. 5. As a consequence, the system of SHE equations becomes nonlinear, which, however, is usually not a concern for self-consistent simulations, because the SHE equations are already coupled nonlinearly to the Poisson equation. Hong et al. investigated the influence of Pauli's exclusion principle and found a notable difference for doping concentrations only above $10^{18}\,\mathrm{cm}^{-3}$, where the fit factor for impurity scattering needs to be modified in order to reproduce the Caughey-Thomas expression for the mobility [32].

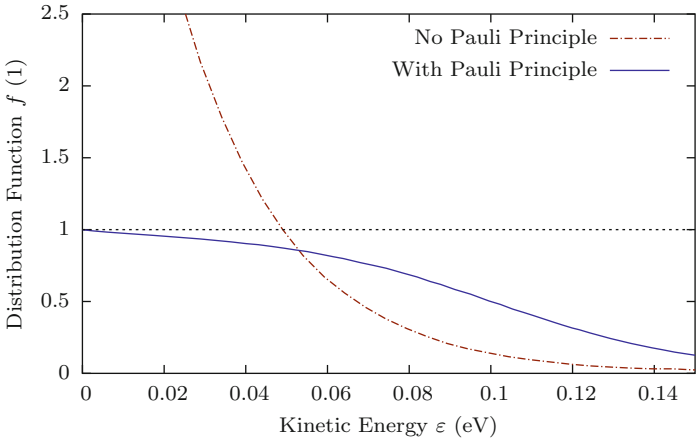

Fig. 5 Comparison of the electron distribution function for a SiGe HBT at room temperature with a maximum doping level of $2 \times 10^{20}\,\mathrm{cm}^{-3}$ in the emitter region [32]. If the Pauli principle is not considered, the distribution function obtains values higher than unity at such extreme doping

4.3 Carrier-Carrier Scattering

Rauch et al. demonstrated in earlier work [33, 34] and also in Chap. 5 [1] that electron-electron scattering results in an increased population of states at high energies, thereby lifting the high-energy tail of the distribution function significantly enhancing HCD. Carrier-carrier scattering is a two carrier process, where the two carriers involved change their individual momentum and energy instantaneously, but conserve the overall momentum and energy. In particular, this interaction may increase the energy of the carrier with higher energy even further, resulting in additional hot carriers particularly in short-channel devices. The elevation of the high-energy tail in turn then increases the probability of a single electron to break, upon interaction, atomic bonds for example at the semiconductor-oxide interface. At the same time, it has been extensively documented [5, 35, 36] that solving the BTE without any electron-electron scattering leads to an underestimation of the hot-carrier degradation. Figure 6 depicts a comparison of the electron and hole acceleration integrals obtained from carrier distribution functions if only phonon (acoustic and optical) and impurity scattering are considered, and acceleration integrals obtained by additionally considering electron-electron scattering.

Similar to the case of Pauli's exclusion principle, the scattering operator in (32) becomes nonlinear if carrier-carrier interaction is considered. Modelling carrier-carrier interaction using a low-density approximation, one obtains

$$\mathcal{Q}\{f\} = \frac{1}{(2\pi)^3} \int_{\mathcal{B}} \int_{\mathcal{B}} \int_{\mathcal{B}} s(\boldsymbol{x}, \boldsymbol{k}^*, \boldsymbol{k}, \boldsymbol{k}_2^*, \boldsymbol{k}_2) f(\boldsymbol{x}, \boldsymbol{k}^*, t) f(\boldsymbol{x}, \boldsymbol{k}_2^*, t) - s(\boldsymbol{x}, \boldsymbol{k}^*, \boldsymbol{k}, \boldsymbol{k}_2^*, \boldsymbol{k}_2) f(\boldsymbol{x}, \boldsymbol{k}, t) f(\boldsymbol{x}, \boldsymbol{k}_2, t)\, \mathrm{d}\boldsymbol{k}^*\, \mathrm{d}\boldsymbol{k}_2\, \mathrm{d}\boldsymbol{k}_2^*. \quad (34)$$

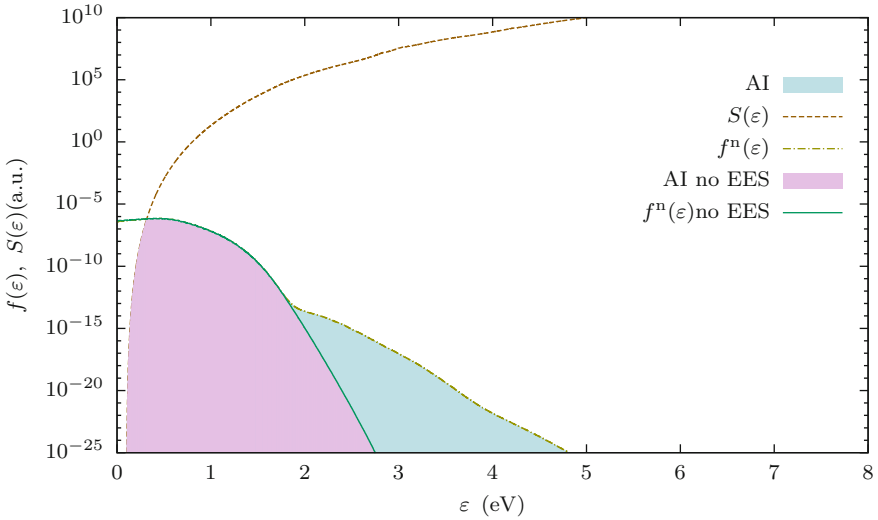

Fig. 6 The influence of electron-electron scattering (EES) on the acceleration integral. The graphical comparison of the acceleration integrals shows the importance of electron-electron scattering for hot-carrier degradation modeling

If also Pauli's inclusion principle is considered, the quadratic nonlinearity then becomes a fourth-order nonlinearity. The carrier-carrier scattering rate $s(\boldsymbol{x}, \boldsymbol{k}^{\text{initial}}, \boldsymbol{k}^{\text{final}}, \boldsymbol{k}_2^{\text{initial}}, \boldsymbol{k}_2^{\text{final}})$ for transition from the two initial states $\boldsymbol{k}^{\text{initial}}$ and $\boldsymbol{k}_2^{\text{initial}}$ to the two final states $\boldsymbol{k}^{\text{final}}$ and $\boldsymbol{k}_2^{\text{final}}$ of the two carriers needs to be such that both energy and momentum is conserved, i.e.

$$s(\boldsymbol{x}, \boldsymbol{k}^{\text{initial}}, \boldsymbol{k}^{\text{final}}, \boldsymbol{k}_2^{\text{initial}}, \boldsymbol{k}_2^{\text{final}}) \sim \\ \delta(\boldsymbol{k} + \boldsymbol{k}^* - \boldsymbol{k}_2 - \boldsymbol{k}_2^*)\delta(\varepsilon + \varepsilon^* - \varepsilon_2 - \varepsilon_2^*) \tag{35}$$

with Dirac distribution δ. This dual conservation property induces additional complications when compared to e.g. phonon scattering processes, where only energy needs to be conserved. Moreover, the strong angular anisotropy of the scattering rate needs to be resolved appropriately. Ventura et al. developed a technique for considering carrier-carrier scattering in a first-order SHE method [37, 38]. Rupp et al. refined the method for use with an arbitrary-order SHE method and verified results for bulk silicon with Monte Carlo results [39]. Due to a non-local coupling of the carrier-carrier scattering operator with respect to energy, which is expected since for a fixed spatial coordinate $\boldsymbol{x}$ all carriers may interact, execution times as well as memory requirements increase by about one to two orders of magnitude depending on the resolution with respect to energy (cf. Fig. 7). For one- and two-dimensional device simulation this increase is usually acceptable considering the amount of main memory available in today's workstations, whereas certain compromises (or compute clusters) may be necessary for fully three-dimensional device simulations.

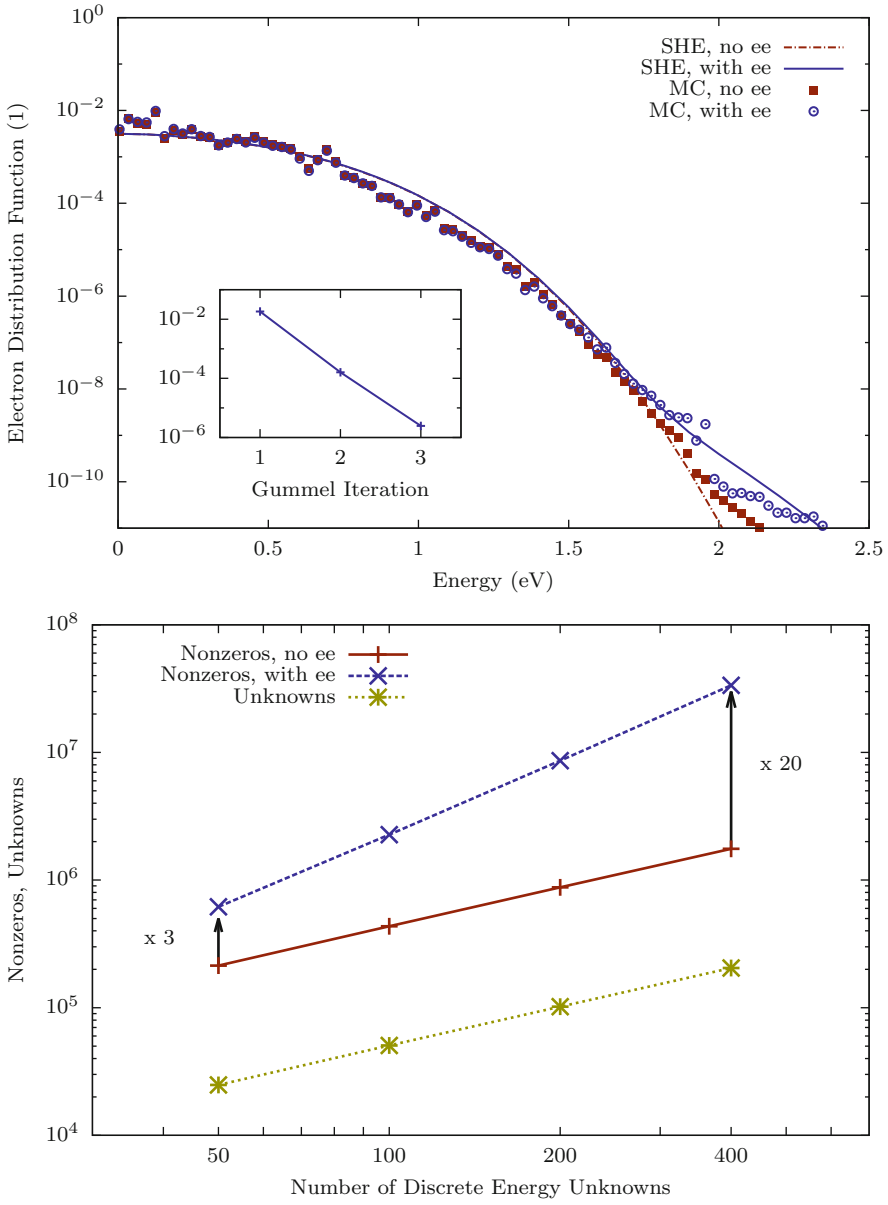

Fig. 7 Comparison of the electron distribution functions with and without electron-electron scattering in a bulk semiconductor including a convergence plot of the electron distribution function at 2 eV (*top*). The number of nonzeros in the system matrix increases quadratically with the number of energy grid points (*bottom*)

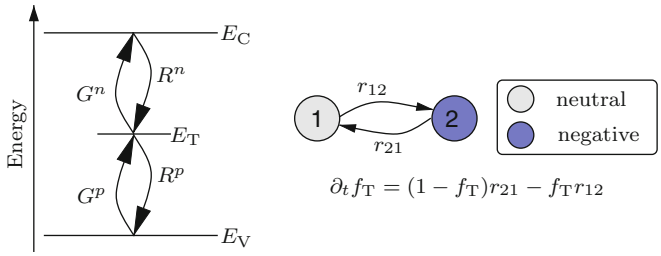

Fig. 8 *Left*: The trap occupancy is governed by a first-order rate equation and two transition rates r_{12} and r_{21}, which are obtained from the four recombination/generation rates shown in the band diagram. The defect can become charged (state 2) by either capturing an electron from the conduction band or by emitting a hole to the valence band and vice versa. *Right*: The two state model of a defect located within the band gap ($E_V < E_T < E_C$), where E_V is the valence band edge energy and E_C is the conduction band edge energy. The defect only carries a charge in state two, which needs to be considered upon solving Poisson's equation

4.4 Generation and Recombination

The scattering operators discussed so far do not consider bipolar effects such as the recombination of an electron-hole pair. In order to be able to consider generation-recombination processes, a separate BTE for electrons and holes is used in (6). This allows for the inclusion of additional details and is needed for fully bipolar devices such as pn-diodes, whereas early approaches coupling the BTE for one carrier type with a continuity equation for the second carrier type, cf. e.g. [40], are less flexible.

Since models for carrier generation and recombination can become quite complex [41], we only deal with the simplest two-state trap (cf. Fig. 8), for which the state of the trap is described by a single trap occupancy f_T and a trap level E_T. Also, we assume spin relaxation to be infinitely fast, such that the trap occupancy is independent of the electron spin. With these assumptions the macroscopic rate equation for the trap occupancy is given by [42, 43]

$$\frac{\partial f_T}{\partial t} = \int_{\mathcal{B}} (1 - f_T) \underbrace{\left(R^n(\boldsymbol{k}') f^n - G^p(\boldsymbol{k}')(1 - f^p)\right)}_{r_{21}} + f_T \underbrace{\left(R^p(\boldsymbol{k}') f^n - G^n(\boldsymbol{k}')(1 - f^n)\right)}_{r_{12}} \mathrm{d}^3\boldsymbol{k}', \tag{36}$$

where $G^n(\boldsymbol{k}')$ and $G^p(\boldsymbol{k}')$ are the number of generated electrons and holes per second per $\mathrm{d}^3\boldsymbol{k}'$, $R^n(\boldsymbol{k}')$ and $R^p(\boldsymbol{k}')$ are the number of recombined electrons and holes per second per $\mathrm{d}^3\boldsymbol{k}'$. With this the recombination operators $\Gamma^{p/n}\{f^n, f^p\}$ for electrons and holes as introduced in (6) read

$$\Gamma^n\{f^n, f^p\} = \frac{N_T}{(2\pi)^3} \int_{\mathcal{B}} G^n(\boldsymbol{k}') f_T (1 - f^n) - R^n(\boldsymbol{k}')(1 - f_T) f^n \, \mathrm{d}^3\boldsymbol{k}', \tag{37}$$

$$\Gamma^{\mathrm{p}}\{f^{\mathrm{n}}, f^{\mathrm{p}}\} = \frac{N_{\mathrm{T}}}{(2\pi)^3} \int_{\mathcal{B}} G^{p}(\boldsymbol{k}')(1 - f_{\mathrm{T}})(1 - f^{\mathrm{p}}) - R^{p}(\boldsymbol{k}')\, f_{\mathrm{T}} f^{\mathrm{p}}\, \mathrm{d}^3\boldsymbol{k}', \tag{38}$$

where N_{T} is the trap concentration. The recombination rates for electrons and holes are [43, 44]

$$R^{\mathrm{n}}(\boldsymbol{k}') = \sigma^{\mathrm{n}} v^{\mathrm{n}}(\boldsymbol{k}') \quad \text{and} \quad R^{\mathrm{p}}(\boldsymbol{k}') = \sigma^{\mathrm{p}} v^{\mathrm{p}}(\boldsymbol{k}'), \tag{39}$$

where σ^{n} and σ^{p} are experimentally determined capture cross sections and v^{n} and v^{p} are reaction velocities for electrons and holes, respectively. From the principle of detailed balance [42, 44] the generation rates are found as

$$G^{\mathrm{n}}(\boldsymbol{k}') = \sigma^{\mathrm{n}} v^{\mathrm{n}}(\boldsymbol{k}') \exp\left(\frac{E_{\mathrm{T}} - E(\boldsymbol{k})}{k_{\mathrm{B}} T}\right), \tag{40}$$

$$G^{\mathrm{p}}(\boldsymbol{k}') = \sigma^{\mathrm{p}} v^{\mathrm{p}}(\boldsymbol{k}') \exp\left(\frac{E(\boldsymbol{k}') - E_{\mathrm{T}}}{k_{\mathrm{B}} T}\right). \tag{41}$$

The expansion into spherical harmonics of equations (37) and (38) utilizing the H-transform results in

$$\begin{aligned}\Gamma^{\mathrm{n}}\{f^{\mathrm{n}}, f^{\mathrm{p}}\}_{l,m} = N_{\mathrm{T}} Z^{\mathrm{n}}(H)\big[&G^{\mathrm{n}}(H) f_{\mathrm{T}}(1 - f^{\mathrm{n}}_{l,m}) \\ &- R^{\mathrm{n}}(H)\Big(\frac{1}{Y_{0,0}} - f_{\mathrm{T}}\Big) f^{\mathrm{n}}_{l,m}\big]\Big)\delta_{l,0}\delta_{l,m},\end{aligned} \tag{42}$$

$$\begin{aligned}\Gamma^{\mathrm{n}}\{f^{\mathrm{n}}, f^{\mathrm{p}}\}_{l,m} = N_{\mathrm{T}} Z^{\mathrm{p}}(H)\big[&G^{\mathrm{p}}(H)\Big(\frac{1}{Y_{0,0}} - f_{\mathrm{T}}\Big)(1 - f^{\mathrm{p}}_{l,m}) \\ &- R^{\mathrm{p}}(H) f_{\mathrm{T}} f^{\mathrm{p}}_{l,m}\big]\delta_{l,0}\delta_{l,m}.\end{aligned} \tag{43}$$

With this the full bipolar system is defined. For further results obtained for a pn-diode we refer the reader to the work by Rupp et al. [45].

5 Hot Carrier Modeling Using the Spherical Harmonics Expansion Method

In this section we demonstrate time-efficient SHE solutions of the bipolar BTE, which are then applied to the investigation of HCD in n-channel MOSFETs. Detailed results in a full HCD context have already been presented in Chap. 8 [2], hence we merely supplement the results already given there. We solve (6) self-consistently on unstructured grids using the free open-source, higher-order spherical harmonics expansion simulator ViennaSHE [45–47]. Full-band effects in silicon are accounted for using the method suggested by Jin et al. [31]. The scattering mechanisms considered are acoustical and optical phonon scattering, impurity scattering,

impact ionization [10] with secondary carrier generation, and electron-electron scattering [39]. To assess the damage caused by hot carriers, the acceleration integral from (1) is recast as

$$G(\boldsymbol{x}_{\mathrm{it}}, t) = \int_{\varepsilon^{\mathrm{th}}}^{\infty} f(\boldsymbol{x}_{\mathrm{it}}, \varepsilon, t) S(\varepsilon)\, \mathrm{d}\varepsilon = \sigma_0 \int_{\varepsilon^{\mathrm{th}}}^{\infty} f(\varepsilon) \underbrace{Z(\varepsilon) \left(\frac{\varepsilon - \varepsilon^{\mathrm{th}}}{1\ \mathrm{eV}} \right)^{p} v_{\mathrm{g}}(\varepsilon)}_{= S(\varepsilon)/\sigma_0}\, \mathrm{d}\varepsilon, \tag{44}$$

and evaluated for electrons and holes along the gate oxide interface at x_{it}. Here, σ_0 is the capture cross section, $p = 11$ is used for a multi-particle process, whereas $p = 1$ is taken for a single particle process, $Z(\epsilon)$ denotes the density of states (DOS), $v_{\mathrm{g}}(\epsilon)$ is the group velocity, and ε is the kinetic energy [48, 49]. The acceleration integral is the kernel of the hot carrier degradation model and is used to describe single- and multiple-carrier bond dissociation processes [48, 50, 51]. To simulate the device degradation in terms of a relative decrease in $I_{\mathrm{d,\,lin}}$, we use the acceleration integrals for electrons and holes in our detailed degradation model [51]. Using this approach, two two-dimensional n-channel MOSFETs with 250 and 25 nm channel lengths subjected to hot carrier stress at high oxide ($\approx$ 8 MV/cm) and lateral electric fields ($\approx$ 1 MV/cm) are investigated to assess the numerical and physical properties of the distribution function and the acceleration integral. Interface states generated at the semiconductor-oxide interface during HCD disturb the electrostatics of the device and affect the carrier mobility. To incorporate these effects in a self-consistent manner, the acceleration integral was evaluated and used within our degradation model [51] to calculate the interface state density N_{it} at each simulation step. Additionally, N_{it} was used for the self-consistent treatment of trapped charges in every step.

5.1 Evaluation of Computational Costs

In order to show the impact and the relative computational effort of the various degrees of sophistication, the 'conventional' BTE with impurity and phonon scattering was used as an initial guess for the subsequent simulations. To achieve accurate and deterministic solutions of the BTE under high-field conditions, the distribution function was first obtained for low-field conditions, considering only phonon and impurity scattering. The obtained solution was in a second step used as an initial guess for the device simulation under high-field conditions, considering only phonon and impurity scattering. In a third step, these results were used to solve the BTE under high-field conditions including electron-electron scattering and impact ionization scattering. Using this procedure, the total simulation time and memory usage was minimized.

The computational cost in terms of execution time is depicted in Fig. 9, while memory requirements are shown in Fig. 10. All simulations have been performed

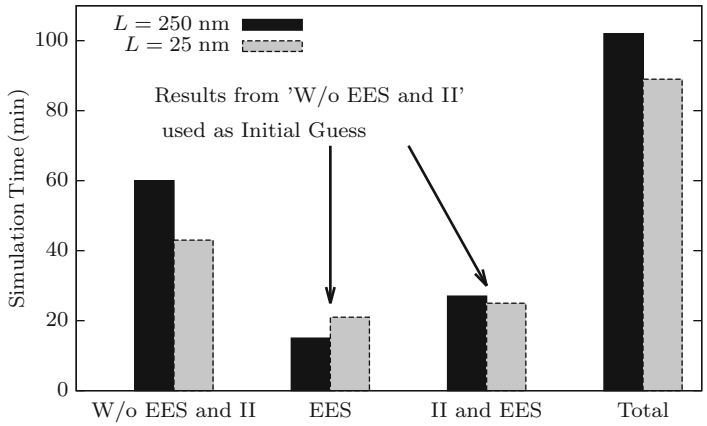

Fig. 9 The time needed to compute the distribution functions for two different device lengths L and the total simulation time. It can be seen that the simulation times without electron-electron scattering (EES) and impact ionization (II) scattering are larger than for those for additionally considering EES and II scattering

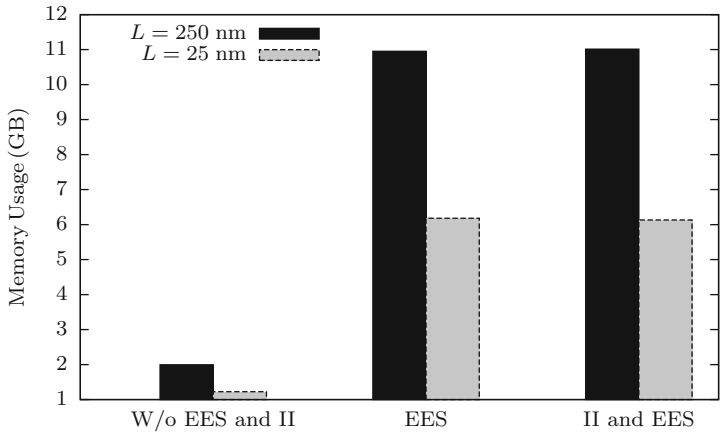

Fig. 10 The total random access memory used for each case. Whilst the simulations incorporating only phonon and impurity scattering took longer than the incremental others, they required considerably less memory (cf. Fig. 9). The most memory was needed for the long channel device ($L = 250$ nm), since more mesh points had to be used. Using electron-electron scattering (EES) results in a significantly higher memory consumption, which is due to the additional coupling introduced by the non-linear EES operator. In contrast, impact ionization (II) scattering does not have a notable influence on the simulation time

using all six cores of an AMD Phenom II X6 1090T Processor with a total memory of 12 GB. From a productivity point of view it is important to emphasize that the simulation results are obtained within minutes, whereas conventional Monte Carlo simulations may take up to several orders of magnitude longer.

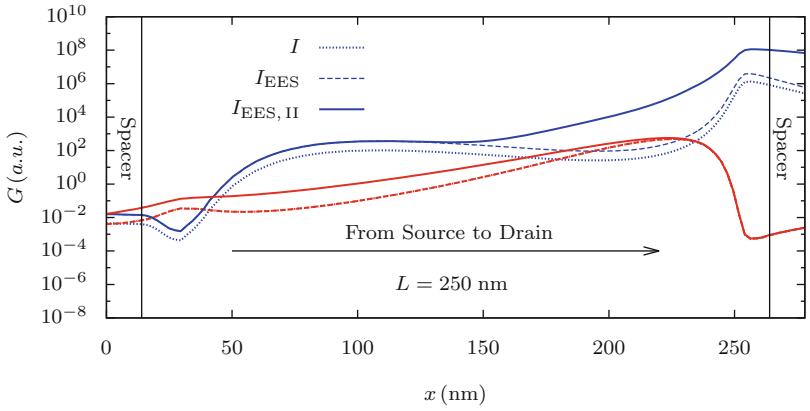

Fig. 11 Plot of the acceleration integrals along the gate oxide interface from source to drain for electrons (*blue*) and holes (*red*), computed from a bipolar solution of the BTE comparing phonon and impurity scattering, impact ionization (II) scattering, and electron-electron scattering (EES) in a 250 nm *n*-channel device under hot-carrier stress

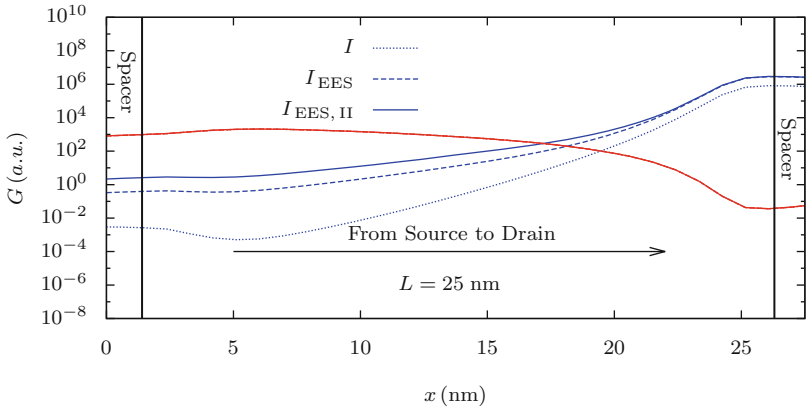

Fig. 12 The acceleration integrals along the gate oxide interface from the source to drain for electrons (*blue*) and holes (*red*) in a 25 nm *n*-channel device. The influence of electron-electron scattering (EES) on the acceleration integral (AI) as compared to the AIs for the long channel device (cf. Fig. 11) is much more significant, whilst the influence of impact ionization (II) is small

5.2 Evaluation of Computational Results

For the short channel device (25 nm) the shift caused by electron-electron scattering and shown in Fig. 11 is significantly higher close to the source as compared to the long channel MOSFET (cf. Fig. 12). Impact ionization causes a dramatic increase in the acceleration integral for electrons in the long channel device (cf. Fig. 11) near the drain and a slight increase of the a for holes near the source. Since there is not enough room for the carriers to lose the attained kinetic energy through scattering

processes in the short channel device, a slight increase of the acceleration integral for electrons near the source and no increase in the acceleration integral for holes is observed. It is interesting to note that when comparing the case of impact ionization with electron-electron scattering with the case where impact ionization was not considered, no further increase in the acceleration integral for electrons close to the drain is obtained in the short channel device (cf. Fig. 12). This can be attributed to the short channel, which does not allow the carriers to gain sufficient energy, and a loss in kinetic energy through electron-electron scattering near the drain.

6 Available Implementations of the SHE Method

From the discussion and results presented in this chapter the SHE method has to be seen as a major enabler for future, refined research and developments in HCD. However, when comparing the SHE method with the established drift-diffusion model or the Monte Carlo method, the substantially higher complexity, both in terms of the underlying mathematical algorithms and the physical details, are a substantial hindrance for wide-spread adoption.

Commercial implementations of selected features of the SHE method are available from Synopsys [52] and Global TCAD Solutions [53]. The closed-source nature of these software packages is only poorly suited for stimulating further research on the SHE method because implementation details are not accessible. For the same reason, they only provide limited extensibility. To mitigate these problems, our work on the simulator ViennaSHE [54] is freely accessible as open source software under a permissive MIT/X11 license. In addition to regular releases, the developer repository is publicly accessible via the web-based hosting service GitHub [55], simplifying the ability to provide feedback or even code contributions substantially.

7 Conclusion

The SHE method is attractive for the study of hot carrier degradation, since it allows for the computation of deterministic solutions of the BTE over many orders of magnitude and free from stochastic noise. Important details such as impact ionization and carrier-carrier scattering can be included at a high level of detail, while simulation times are only in the order of minutes or hours.

Acknowledgements The authors wish to thank P. Palestri and A. Zaka for providing Monte Carlo data for carrier-carrier scattering. Support by the Austrian Science Fund (FWF), grant P23598, is gratefully acknowledged.

References

1. S.E. Rauch, F. Guarin, The energy driven hot carrier model, in *Hot Carrier Degradation in Semiconductor Devices*, ed. by T. Grasser. (Springer, Cham, 2014)
2. S. Tyaginov, Physics-based modeling of hot-carrier degradation, in *Hot Carrier Degradation in Semiconductor Devices*, ed. by T. Grasser. (Springer, Cham, 2014)
3. S. Tyaginov, I. Starkov, C. Jungemann, H. Enichlmair, J. Park, T. Grasser, in *Proceedings of ESSDERC*, pp. 151–154 (2011)
4. S. Tyaginov, I. Starkov, O. Triebl, J. Cervenka, C. Jungemann, S. Carniello, J. Park, H. Enichlmair, M. Karner, C. Kernstock, E. Seebacher, R. Minixhofer, H. Ceric, T. Grasser, in *Proceedings of IPFA*, pp. 1–5 (2010)
5. M. Bina, K. Rupp, S. Tyaginov, O. Triebl, T. Grasser, in *IEEE International Electron Devices Meeting (IEDM)*, pp. 30.5.1–30.5.4 (2012)
6. W. McMahon, A. Haggag, K. Hess, IEEE Trans. Nanotechnol. **2**(1), 33 (2003)
7. A. Zaka, P. Palestri, Q. Rafhay, R. Clerc, D. Rideau, L. Selmi, Semi-analytic modeling for hot carriers in electron devices, in *Hot Carrier Degradation in Semiconductor Devices*, ed. by T. Grasser. (Springer, Cham, 2014)
8. S. Reggiani, G. Barone, E. Gnani, A. Gnudi, G. Baccarani, S. Poli, R. Wise, M.Y. Chuang, W. Tian, S. Pendharkar, M. Denison, Characterization and modeling of high-voltage LDMOS transistors, in *Hot Carrier Degradation in Semiconductor Devices*, ed. by T. Grasser. (Springer, Cham, 2014)
9. S.M. Hong, C. Jungemann, J. Comput. Electron. **8**, 225 (2009)
10. C. Jungemann, B. Meinerzhagen, *Hierarchical Device Simulation*. Computational Microelectronics (Springer, Wien, 2003)
11. B. Meinerzhagen, A. Pham, S.M. Hong, C. Jungemann, in *International Conference on Simulation of Semiconductor Processes and Devices (SISPAD)*, pp. 293–296 (2010)
12. A. Bravaix, C. Guerin, V. Huard, D. Roy, J. Roux, E. Vincent, in *IEEE International Reliability Physics Symposium*, pp. 531–548 (2009)
13. C. Guerin, V. Huard, A. Bravaix, J. Appl. Phys. **105**(11), 114513 (2009)
14. A. Bravaix, V. Huard, F. Cacho, X. Federspiel, D. Roy, Hot-carrier degradation in decananometer CMOS nodes: from an energy driven to a unified current degradation modeling by multiple carrier degradation process, in *Hot Carrier Degradation in Semiconductor Devices*, ed. by T. Grasser. (Springer, Cham, 2014)
15. N. Goldsman, C. Lin, Z. Han, C. Huang, Superlattices Microstruct. **27**, 159 (2000)
16. S. Hong, A. Pham, C. Jungemann, *Deterministic Solvers for the Boltzmann Transport Equation* (Springer, Wien, 2011)
17. C. Herring, E. Vogt, Phys. Rev. **101**(3), 944 (1956)
18. C. Jungemann, A.T. Pham, B. Meinerzhagen, C. Ringhofer, M. Bollhöfer, J. Appl. Phys. **100**(2), 024502 (2006)
19. H. Kosina, M. Harrer, P. Vogl, S. Selberherr, in *Proceedings of SISDEP*, pp. 396–399 (1995)
20. S.M. Hong, C. Jungemann, in *Proceedings of ESSDERC*, pp. 170–173 (2008)
21. D. Schroeder, D. Ventura, A. Gnudi, G. Baccarani, Electron. Lett. **28**(11), 995 (1992)
22. K. Rahmat, J. White, D.A. Antoniadis, IEEE Trans. Comput. Aided Des. Integr. Circuits Syst. **15**(10), 1181 (1996)
23. C. Ringhofer, Trans. Theory Stat. Phys. **31**, 431 (2002)
24. A. Gnudi, D. Ventura, G. Baccarani, F. Odeh, Solid State Electron. **36**(4), 575 (1993)
25. R. Brunetti, C. Jacoboni, F. Nava, L. Reggiani, G. Bosman, R. Zijlstra, J. Appl. Phys. **52**(11), 6713 (1981)
26. C. Jacoboni, P. Lugli, *The Monte Carlo Method for Semiconductor Device Simulation* (Springer, Wien, 1989)
27. R. Brunetti, Solid State Electron. **32**, 1663 (1989)
28. A.T. Pham, C. Jungemann, B. Meinerzhagen, in *Proceedings of SISPAD*, pp. 361–364 (2006)
29. G. Matz, S.M. Hong, C. Jungemann, in *Proceedings of SISPAD*, pp. 167–170 (2010)

30. M.C. Vecchi, D. Ventura, A. Gnudi, G. Baccarani, in *Proceedings of NUPAD*, pp. 55–58 (1994)
31. J. Seonghoon, S. Hong, C. Jungemann, IEEE Trans. Electron Devices **58**(5), 1287 (2011)
32. S.M. Hong, C. Jungemann, in *Proceedings of SISPAD*, pp. 135–138 (2010)
33. S. Rauch, F. Guarin, G. La Rosa, IEEE Electron Devices Lett. **19**(12), 463 (1998)
34. S. Rauch, G. La Rosa, F. Guarin, IEEE Trans Devices Mater. Reliab. **1**(2), 113 (2001)
35. A. Zaka, P. Palestri, Q. Rafhay, R. Clerc, M. Iellina, D. Rideau, C. Tavernier, G. Pananakakis, H. Jaouen, L. Selmi, IEEE Trans. Electron Devices **59**(4), 983 (2012)
36. S. Tyaginov, M. Bina, F. Jacopo, D. Osintsev, Y. Wimmer, B. Kaczer, T. Grasser, in *IEEE International Integrated Reliability Workshop Final Report* (2013)
37. A. Ventura, D. Gnudi, , G. Baccarani, in *Proceedings of SISDEP*, pp. 161–164 (1993)
38. D. Ventura, A. Gnudi, G. Baccarani, F. Odeh, Appl. Math. Lett. **5**(3), 85 (1992)
39. K. Rupp, P.W. Lagger, T. Grasser, A. Jungel, in *Proceedings of IWCE*, pp. 1–4 (2012)
40. H. Lin, N. Goldsman, I.D. Mayergoyz, in *Proceedings of IWCE*, pp. 143–146 (1992)
41. T. Grasser, Microelectron. Reliab. **52**(1), 39 (2012)
42. O. Madelung, *Introduction to Solid-State Theory*. Springer Series in Solid-State Sciences (Springer, New York, 1996)
43. A. Piazza, C. Korman, A. Jaradeh, IEEE Trans. Comput. Aided Des. Integr. Circuits Syst. **18**(12), 1730 (1999)
44. W. Shockley, W.T. Read, Phys. Rev. **87**, 835 (1952)
45. K. Rupp, C. Jungemann, M. Bina, A. Jüngel, T. Grasser, in *Proceedings of SISPAD*, pp. 19–22 (2012)
46. K. Rupp, T. Grasser, A. Jüngel, in *IEDM Technical Digest* (2011)
47. K. Rupp, T. Grasser, A. Jüngel, in *Proceedings of SISPAD*, pp. 151–155 (2011)
48. W. McMahon, A. Haggaag, K. Hess, IEEE Trans. Nanotechnol. **2**(1), 33 (2003)
49. S. Tyaginov, I. Starkov, H. Enichlmair, J. Park, C. Jungemann, T. Grasser, ECS Trans. **35**(4), 321–352 (2011). Online: http://ecst.ecsdl.org/content/35/4/321.abstract
50. A. Bravaix, V. Huard, in *European Symposium on the Reliability of Electron Devices* (2010)
51. S. Tyaginov, I. Starkov, O. Triebl, H. Enichlmair, C. Jungemann, J. Park, H. Ceric, T. Grasser, in *Proceedings of SISPAD*, pp. 123–126 (2011)
52. Synopsys Inc. Online: http://www.synopsys.com/
53. Global TCAD Solutions. Online: http://www.globaltcad.com/
54. ViennaSHE Device Simulator. Online: http://viennashe.sourceforge.net/
55. ViennaSHE Developer Repositories. Online: http://github.com/viennashe/